Hindawi
Structural Control and Health Monitoring
Volume 2024, Article ID 9922305, 19 pages
https://doi.org/10.1155/2024/9922305

Research Article

A Novel Enhanced Torsional Eddy Current Damper for Fixed-Axis Rotation Control of Rigid Bodies

Shuai Wang,[1,2,3,4] **Zhengqing Chen**,[1,3,4] **Wenxi Wang**,[1,3,4] **Tianfu Yu**,[3,4] **Hongyi Zhang**,[1,3,4] **and Xugang Hua**[1,3,4]

[1]*National Key Laboratory of Bridge Safety and Resilience, Hunan University, Changsha 410082, China*
[2]*College of Mechanical and Vehicle Engineering, Hunan University, Changsha 410082, Hunan, China*
[3]*Key Laboratory for Bridge and Wind Engineering of Hunan Province, Hunan University, Changsha 410082, Hunan, China*
[4]*Vibration and Shock Technology Research Center, Hunan University, Changsha 410082, Hunan, China*

Correspondence should be addressed to Wenxi Wang; wxwang@hnu.edu.cn

Received 17 July 2023; Revised 3 January 2024; Accepted 23 January 2024; Published 21 February 2024

Academic Editor: Zili Zhang

The control of angular velocities in the fixed-axis rotation of rigid bodies is crucial for ensuring the safety and functionality of civil structures and mechanical systems. In this research, a novel enhanced torsional eddy current damper (ETECD) is proposed to effectively control the angular velocities of rigid bodies within confined installation spaces. At first, an estimation approach is developed to determine the damping coefficient of the eddy current damper (ECD) within limited installation space. Furthermore, we utilize a gearbox to enhance the damping performance of the ECD in confined spaces. To establish the framework for the design of the proposed ETECD, the motion equation and solution of the rotating body are derived. By analytically presenting the approximate solution for the responses of a rotating body with a torsional viscous damper, the required range of the torsional damping coefficient is derived. This range ensures compliance to velocity restrictions under linearly angle-related torques, guiding the design of the ETECD. The ETECD, comprising two cylindrical torsional eddy current dampers (ECDs) and a motion-amplified gearbox, is designed and tested for a rotating body. Numerical examples and experimental tests are carried out to validate the performance of the proposed ETECD. The calculated damping coefficients and predicted control performance in the numerical examples agree well with the experimental results. Notably, under the minimum and maximum torques, the terminal angular velocity (TAV) of the rotating body can be significantly reduced by 70.76% and 58.99%, respectively. The proposed work emphasizes the potential of the ETECD as an effective and economic method in reducing angular velocities for rotating bodies.

1. Introduction

The rigid rotating body holds great significance as a mechanical component in civil structures and mechanical systems [1–4]. However, excessive angular velocities in these rotating bodies can lead to significant impacts on supporting members, resulting in structural damages or even failures [5–9]. The control of vibration and buffering in rotational motion is mainly divided into two categories. One approach involves control by reducing the load that generates vibrations, such as optimizing machining strategies in mechanical processing [10], and refining methods for crane motion switching [11]. The second category involves the use of vibration-reducing devices to recover and dissipate energy. Common research includes studies on rotational vibration control to harvest energy, such as converting human body vibrations into rotational motion for power generation and energy recovery [12] and transforming car vibrations into rotational motion for energy recovery [13]. In civil engineering, there are also studies on utilizing rotation to dissipate structural energy for vibration control. For example, Huang et al. [14] investigated the effectiveness of rotational inerter dampers in structural vibration control. Wang et al. [15] explored the effects of rotational amplification brackets on the vibration control of frame structures. Lin et al. [16] studied the combined effects of lateral dampers and rotational dampers on cable vibration control.

The opening process of grille rudders or grid fins in missiles and reusable rockets is a typical example, such as the grid fins opening during the recovery phase of the Falcon 9 first-stage rocket, as illustrated in Figure 1 [17]. If the rotating velocity of the grid fins is excessively high, there is a risk of damage during the final stage of the opening process. Similar situations may occur on glass doors under strong winds. A fracture accident of a rotating glass door happens under a wind speed of 16 m/s in 2021 [18], as shown in Figure 2. It can be seen that the glass door pounds on the fixed frame resulting in a fracture accident. Hence, effective control of angular velocities in rigid rotating bodies is essential to ensure the safety and functionality of fixed-axis rotation systems.

To address the issue of angular velocity in rotating bodies, additional dampers are commonly employed to provide damping capability and ensure structural safety and functionality [19–22]. These dampers are typically installed in the torsional direction of the rotating shaft [23–25]. Displacement-dependent and velocity-dependent dampers are two widely used types of damping devices [26–28]. However, the damping forces generated by displacement-dependent dampers, such as friction dampers [29, 30] and metal dampers [31–33], exhibit nearly constant values. This characteristic leads the rotating bodies from opening or closing as required under small loads [34, 35]. On the other hand, velocity-dependent dampers offer a solution to overcome this limitation, as their damping forces are related to the angular velocity [36–38]. Among velocity-dependent dampers, fluid-based dampers are the most commonly used due to their simplicity and cost-effectiveness [20, 39–41]. However, the way friction generates damping forces may degrade their performance during use. This can also complicate later-stage simulations [42–44].

Recently, eddy current dampers (ECDs) have been reported as another effective velocity-dependent damper for consuming kinetic energy in dynamical systems [45–48]. ECDs offer competitive advantages, such as their noncontact nature, minimal reliance on temperature, approximately linear viscous damping across a broad range of velocities, and long operational lifespan [42, 49, 50]. In its simplest configuration, an ECD comprises a conductive sheet and a permanent magnet (PM) [51–53]. As the conductive sheet and the PM experience relative motion, eddy currents are induced within the sheet. The interplay between these eddy currents and the magnetic fields generated by the PM yields an eddy current damping force that is directly proportional to the relative velocity [50, 54, 55]. Irazu and Elejabarrieta [55] provide a new inverse method to numerically determine the dynamic properties of the contactless eddy current damper. Moreover, Lu et al. [56] have demonstrated the effective reduction of displacement response and acceleration response through the utilization of EC-TMD (eddy current tuned mass damper).

Generally, the requirement for installation space increases with the magnitude of the damping force provided by ECDs [50]. However, due to space limitations and the small damping force at low relative velocities between the conductive sheet and PMs [48, 57], there is a need to develop ECDs with motion amplifiers to amplify relative velocities between the conductive sheet and PMs, which can increase damping efficiency of ECDs. Motion amplification equipment includes gear sets, gear racks, ball screws, etc. The high-speed rotation occurs in these devices, leading to the amplification of inertial mass, and this effect needs to be taken into account. In 1973, Kawamata proposed a liquid mass pump by using the rotational inertial mass of fluid to generate the inertance [58]. This is an early application of inerters in the field of structural vibration control. Recently, Smith elucidated the role of inerter from the perspective of force-electricity contrast and systematically expounded the concept of an inerter, making significant contributions in fields of automation [59]. Following these above, gears and similar speed-increasing mechanisms have found extensive use in inerter control systems [60–62]. Wagg summarized the nonlinear behavior of inerter systems in mechanical systems, categorizing them and proposing future research directions in oscillatory systems [61]. Subsequently, Wagg et al. researched the application of inerter systems in structural engineering such as building and cable vibration control [63–65]. Meanwhile, Zhao and Zhang et al. employed an energy-based approach to clarify the observed advantages of inerter systems [60]. Furthermore, their studies focused on the impact of tuned liquid inerter systems [66] and tuned inerter mass systems [62, 67, 68] in vibration control. Currently, some speed-increasing devices are being applied in eddy current dampers. For instance, a full-scale ECD incorporating a ball screw device was successfully implemented to mitigate longitudinal vibrations in the Zhangjiajie Suspension Bridge [50]. Following that, a modified approach was utilized to conduct an investigation aimed at determining the damping coefficients of ECDs equipped with ball screw devices to effectively control multimode high-order vibrations in the stay cables of the Sutong Bridge [57, 69].

The conventional ECDs discussed earlier were primarily designed to reduce the translational motion and are not suitable for controlling the rotational motion. Meanwhile, an estimation method for the rapid calculation of the damping performance of ECDs based on the limitation of installation space is lacked. Additionally, existing rotational energy dissipation devices [15–17] cannot provide high-efficient damping effects in confined spaces. More importantly, the damping force of most velocity-related dampers is generated from friction, which may deteriorate its performance during usage and make simulations more challenging. In this research, a novel enhanced torsional eddy current damper (ETECD) is introduced as a solution for effectively controlling rotational motion. In the device, a gearbox is employed to amplify the relative velocity between the conductive sheet and PMs for damping enhancement of the torsional ECD. Meanwhile, an estimation approach for determining the damping coefficient of each cylindrical torsional ECD under limited installation space is developed based on the magnetic circuit law. By utilizing the motion equation, an approximate solution is presented and numerically validated for the responses of a rotating body equipped with a torsional viscous damper. This analytical

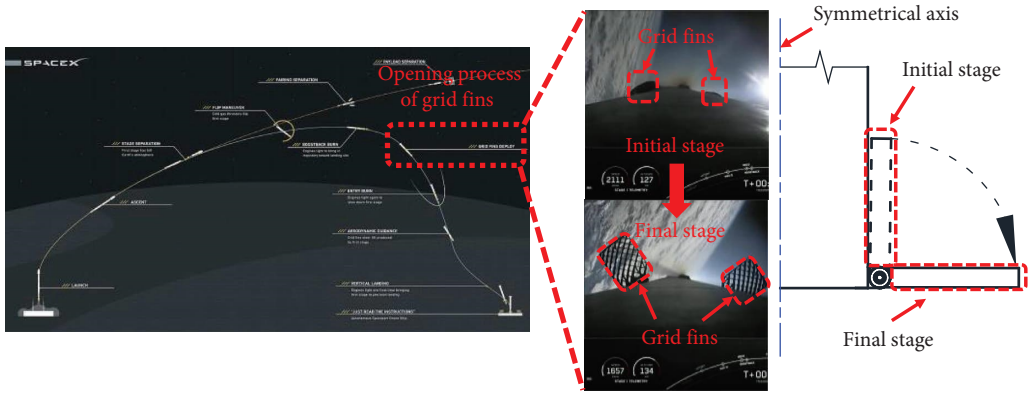

Figure 1: Opening process of the grid fins during Falcon 9 first-stage rocket recovery [17].

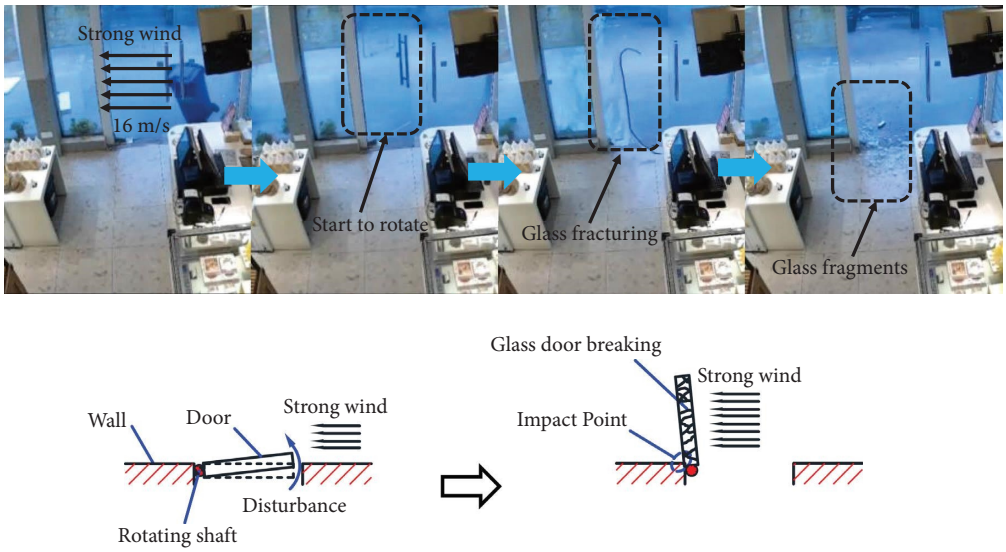

Figure 2: Destroying of a glass door under strong wind.

derivation enables the determination of the required range for the torsional damping coefficient, ensuring compliance with velocity restrictions under arbitrary angle-related torques within the load range. This is of engineering significance for condition requiring velocity-type dampers in rotational motion control where installation space is limited. Moreover, the gearbox is economic and easy to manufacture, and the amplified damper needs fewer permanent magnets and conductors than the conventional ECD. Building upon these findings, two small-scale cylindrical torsional ECDs and a gearbox are designed and manufactured as the principal components of the proposed ETECD. Experimental tests are conducted to examine the control performance of the ETECD.

2. The Proposed Enhanced Torsional Eddy Current Damper (ETECD)

As previously noted, the cylindrical torsional ECD, depicted in Figure 3, acts as the main component of the proposed enhanced torsional eddy current damper (ETECD). Figure 3 illustrates that the cylindrical torsional ECD consists of two main parts: arc-shaped PMs evenly distributed around the circumference with their corresponding back iron as the first part and the conductor tube with its corresponding back iron as the second part.

During relative rotation between the conductor and the PMs, the conductor tube generates eddy currents. These eddy currents interact with the magnetic field produced by the PMs, resulting in an eddy current damping force that is directly proportional to the relative velocity. The torsional damping torque of the ECD is obtained by multiplying this damping force with the radius of the rotation surface. Here, the radius of the rotation surface represents the distance between the outer surface of the PMs and the center of the torsional ECD. In this context, the parameter D represents the diameter of the cylindrical torsional ECD, while L corresponds to its length.

Typically, electromagnetic finite element modeling (FEM) accurately computes the damping torque from ECD. However, FEM computation is time-consuming due to the variation of the modeling parameters. In the initial design

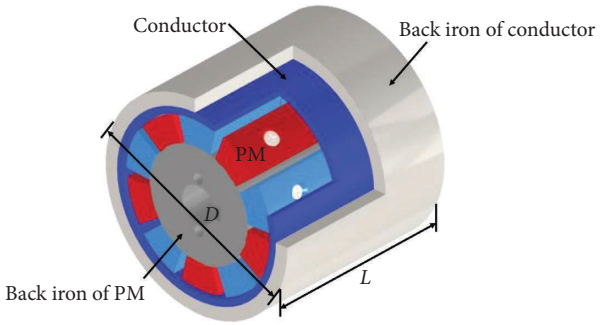

Figure 3: Three-dimensional graph of a cylindrical torsional ECD.

stages, it is essential to develop a concise formula for a quick estimation of the ECD's damping coefficient, addressing diverse spatial limitations in various installations. In this section, a simplified formula is derived considering an installation space of diameter D and length L for the ECD, as shown in Figure 3.

2.1. Calculation of Eddy Current Damping Force at Low Velocity. The magnetic flux in a magnetic field is mainly determined by magnetomotive force and magnetic resistance:

$$\Phi = \frac{T}{\mathfrak{R}}, \tag{1}$$

where Φ is the magnetic flux of the magnetic circuit, T is the magnetomotive force, and R is the magnetic resistance.

For a PM with a thickness of t_m and a residual magnetic flux density of B_{re}, the magnetomotive force T_m can be written as

$$T_m = \frac{B_{re} t_m}{\mu_0}, \tag{2}$$

where μ_0 is the permeability of the vacuum.

The front view of the torsional ECD with PMs is shown in Figure 4. The magnetic circuit of the torsional ECD can be roughly simplified into several magnetic circuit units. Each unit of the magnetic circuit is shown in Figure 5(a), and its equivalent magnetic circuit model is illustrated in Figure 5(b). The distance between neighboring PMs is defined as d_m. Since both the back irons of the conductor and PMs are made of steel materials with negligible magnetic resistance. Therefore, the magnetic resistance $\mathfrak{R}_t$ in the magnetic circuit is mainly related to the thickness of the conductor tube t_c, the thickness of the permanent magnet t_m, and the air gap t_a. It can be expressed as

$$\mathfrak{R}_t = 2\frac{t_m}{\mu_{rm}\mu_0 A} + 2\frac{t_a}{\mu_0 A} + 2\frac{t_c}{\mu_0 A}, \tag{3}$$

where $t_c = R_b - R_c, t_a = R_c - R_m, t_m = R_m - R_d$, and μ_{rm} is the relative permeability of the PM. The equivalent magnetic area A is equal to half of the average surface area A_m, as expressed by $A = A_m/2$. The average surface area is given by $A_m = (W_{mo} + W_{mi})\cdot L/2$, where W_{mo} and W_{mi} are the arc length of the inner and outer cylindrical surface of the PMs, respectively.

Based on the law of the magnetic circuit, the magnetic flux density B can be calculated by

$$B = \frac{\Phi}{A} = 2\frac{T}{\mathfrak{R}_t A} = \frac{B_{re} t_m}{t_m/\mu_{rm} + t_a + t_c}. \tag{4}$$

Therefore, the expression of the damping force of torsional ECD can be obtained from

$$F_\tau = \int J \times \mathrm{BdV} = \int \sigma v B^2 dV = c_\tau v_\tau = 2pA_m t_c \sigma v_\tau \left(\frac{B_{re} t_m}{(t_m/\mu_{rm}) + t_a + t_c}\right)^2, \tag{5}$$

where p is the number of magnetic poles, σ is the conductivity of the conductor tube, c_τ is the damping coefficient in the tangential direction, and v_τ is the relative velocity of the rotation surface in the tangential direction.

2.2. Approximate Calculation of Damping Coefficient of Torsional ECD. Considering the small size of the air gap, we assume that the radius R_m of PMs is approximately equal to R_c. Therefore, we have $v_\tau = \omega \cdot R_m$. Based on the simplified calculation of damping force at low velocity, the damping coefficient c of torsional ECD can be calculated by

$$c = 2pA_m t_c \sigma \left(\frac{B_{re} t_m}{(t_m/\mu_{rm}) + t_a + t_c}\right)^2 \times R_m^2. \tag{6}$$

To ensure all the magnetic induction wire passes through the conductor tube, the distance between PMs (d_m) is assumed to be equal to two times the sum of the thickness conductor t_c and air gap t_a, i.e., $d_m = 2(t_c + t_a)$. In this configuration, a larger damping coefficient can be obtained.

Based on the assumption mentioned above, A_m can be rewritten as

$$A_m = \frac{W_{mo} + W_{mi}}{2} \times L = \left[\pi\left(R_m + R_d\right) - 4p\left(t_c + t_a\right)\right] \times L. \tag{7}$$

Substituting (7) into (6), the damping coefficient c of torsional ECD under the size limitation determined by D and L can be obtained from

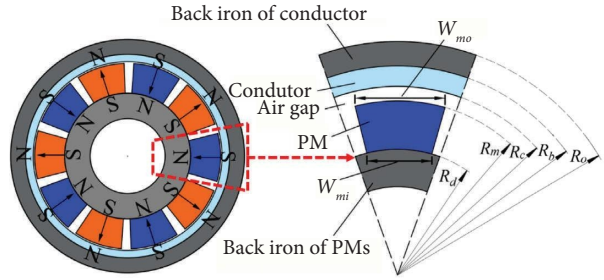

Figure 4: Front view and geometric parameters of the ECD.

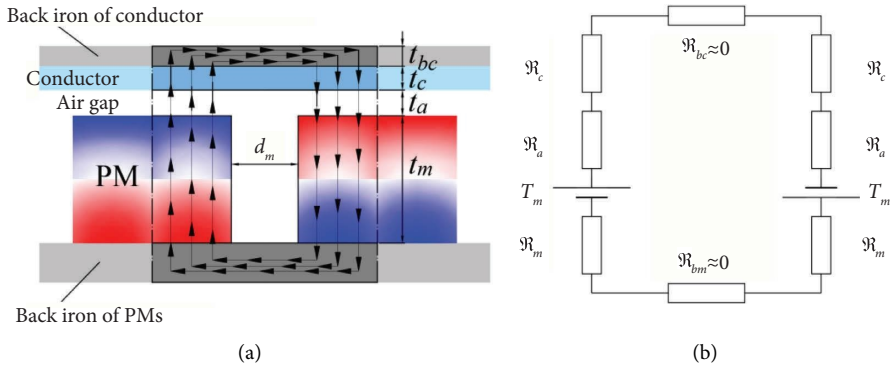

Figure 5: Single equivalent magnetic circuit model of torsional ECD. (a) Magnetic circuit and magnetic flux direction. (b) Equivalent model.

$$c = \sigma t_c R_m^2 \times \left(\frac{B_{re} t_m}{(t_m/\mu_{rm}) + t_a + t_c} \right)^2 \times [\pi (R_m + R_d) - 4p(t_c + t_a)] \times L, \tag{8}$$

where σ is the conductivity of the conductor tube, $R_m = (D - 2(t_a + t_c + t_{bc}))/2$, $t_{bc} = R_o - R_b$, the units of D and L are m, respectively.

According to (8), an analysis is conducted to study the influence of different parametric combinations on the damping coefficient of torsional ECD. Here, B_{re} is set to 1.4 T, μ_{rm} is set to 1.04, $2p$ is set to 10, and t_{bc} is set to 5 mm to satisfy the strength requirements. Initially, a copper conductor tube with a thickness t_c of 2 mm is adopted. The thickness of the PMs t_m is set as 10 mm, and the air gap t_a is set to 1 mm for the convenience of installation. The variation of the damping coefficient (c) with the space limitations (D and L) is shown in Figure 6(a). Furthermore, with D and L set, respectively, to 100 mm and 200 mm, the damping coefficient c varied with t_m, t_a, and t_c which are also displayed in Figure 6.

In Figure 6(a), the damping coefficient (c) of the torsional ECD reaches up to 100 N·m·s/rad when the diameter D is set at 150 mm and the length L at 400 mm. Moving on to Figure 6(b), the damping coefficient rapidly decreases with the increase of air gap (t_a). Meanwhile, the damping coefficient increases with the thickness of the permanent magnets (PMs); however, the rate of increase gradually slows down. When the thickness of the permanent magnet reaches 15 mm, the damping coefficient remains essentially constant. Figure 6(c) provides insights into an optimal value for the conductor tube thickness t_c that maximizes the damping coefficient c. Finally, Figure 6(d) illustrates that, when an optimal value of t_c is selected, c maintains a higher magnitude within the range of 5 to 20 mm for the thickness of the PMs t_m.

2.3. Motion-Amplified Device. The design of the damper for rotating bodies typically involves occupied space while meeting functional requirements. Although the damping coefficient can reach up to 100 N·m·s/rad with $D = 150$ mm and $L = 400$ mm, it is relatively low for most smaller sizes of the ECD. Relying solely on the cylindrical torsional ECD may not provide sufficient damping capacity for structures with demanding damping requirements. In such cases, it becomes necessary to combine ECDs with motion-amplifying devices, which amplify the relative motion between the conductor and PMs, as well as the damping coefficient of the ECDs. In this research, a gearbox is employed as the motion-amplifying device due to its structural simplicity and cost-effectiveness. This combination allows for enhancing the damping coefficient of the cylindrical ECD. Then, the damping coefficient of the cylindrical ECD can be enhanced by

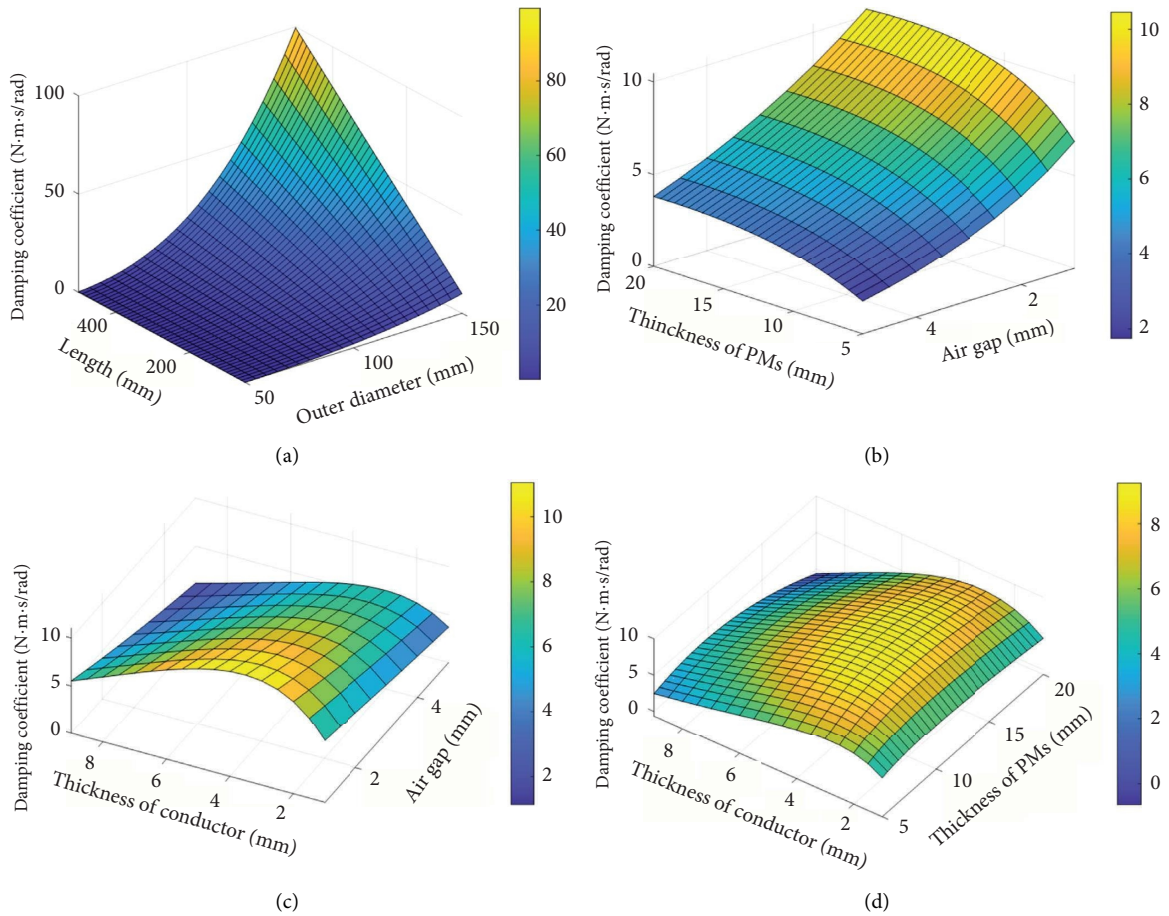

Figure 6: Damping coefficient c varies with different parameters of the ECD. (a) Combinations of length L and outer diameter D. (b) Combinations of the thickness of PMs t_m and air gap t_a ($t_c = 2$ mm). (c) Combinations of the thickness of conductor t_c and air gap t_a ($t_m = 10$ mm). (d) Combinations of the thicknesses of PMs t_m and conductor t_c ($t_a = 1$ mm).

$$c_a = k^2 \times c, \tag{9}$$

where k is the amplification factor of the gearbox. A structural configuration of gears in a typical two-stage motion-amplified gearbox is shown in Figure 7. The input torque and angular velocity are T_1 and ω_1, respectively. The output torque and angular velocity are T_4 and ω_4, respectively. The amplification factor k of the two-stage gearbox can be obtained by

$$k = \frac{Z_1}{Z_2} \times \frac{Z_3}{Z_4}, \tag{10}$$

where Z_1, Z_2, Z_3, and Z_4 are the number of teeth of four gears, respectively. The relationship between T_1 and T_4 and ω_1 and ω_4 can be calculated by

$$\begin{cases} T_1 = k \times T_4, \\ \omega_4 = k \times \omega_1. \end{cases} \tag{11}$$

To enhance the damping capacity of the cylindrical torsional ECD, it is essential to determine an appropriate amplification factor k. However, before delving into the design of the proposed ETECD, it is crucial to derive the motion equation and subsequently determine a solution for the rotating body.

3. Motion Equation and Approximate Solution

3.1. Motion Equation. For operational purposes, rigid rotating bodies, such as grille rudders or grid fins in missiles and reusable rockets, need to achieve rotational motion ranging from 0° to 90°. To ensure smooth operation, a velocity-dependent damper is usually installed between the rotating body and the fixed rotating shaft. Figure 8 illustrates the schematic representation of the mechanical model, which shows a rotating body equipped with a velocity-dependent damper. The motion equation governing the behavior of the rotating body can be expressed as follows:

$$I\ddot{\theta} + c\dot{\theta} = M_L = h\theta, \tag{12}$$

where c is the torsional damping coefficient; θ is the rotational angle; h is the proportional loading coefficient related to the angular displacement; M_L is linearly angle-related torque; I represents the total rotational inertial mass of the entire system, including the rotating body and the amplified parts of the ETECD. The amplified parts of the ETECD

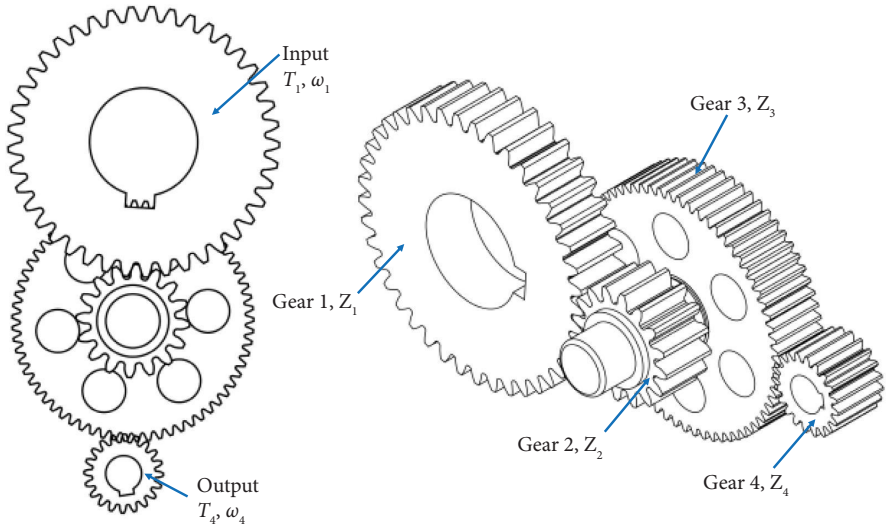

FIGURE 7: Configuration of gears in a typical two-stage gearbox.

include four parts: the rotational inertial mass of Gear2, Gear3, and their shaft (I_{g23}), the rotational inertial mass of Gear4 and its shaft (I_{g4}), the rotational inertial mass of PMs' back iron (I_{bm}), and the rotational inertial mass of the PMs (I_m). The total system's rotational inertial mass is given by

$$I = I_0 + \left(\frac{Z_1}{Z_2}\right) I_{g23} + \left(\frac{Z_1}{Z_2} \times \frac{Z_3}{Z_4}\right)\left(I_{g4} + I_{bm} + I_m\right), \quad (13)$$

where I_0 represents the rotational inertial mass of the rotating body.

In this study, the initial conditions are assumed as follows:

$$\begin{cases} \theta(0) = 0, \\ \dot{\theta}(0) = \omega_0, \end{cases} \quad (14)$$

where ω_0 is the initial angular velocity.

In designing the torsional damping coefficient, two extreme cases are considered. Case 1 involves $M_L = M_{L\min} = h_{\min} \cdot \theta$, where $M_{L\min}$ represents the minimum external torque determined by operational requirements. Similarly, in Case 2, $M_L = M_{L\max} = h_{\max} \cdot \theta$, where $M_{L\max}$ represents the maximum external torque.

It is crucial to establish a reasonable value for the torsional damping coefficient. Setting the damping coefficient too high, while considering friction, makes the rotation process of the rigid body during normal operations challenging. Conversely, if the damping coefficient is too low, the rotating system may sustain damage due to excessive terminal angular velocity (TAV). Here, the TAV is defined as the angular velocity of the rigid body after a 90° rotation. Therefore, within the limitation imposed by the TAV [$\omega'_{\min}$, $\omega'_{\max}$], a satisfactory range for the torsional damping coefficient can be determined. The symbols $\omega'_{\min}$ and $\omega'_{\max}$ represent the preset minimum and maximum TAV values, respectively, depending on the operational requirements.

The TAV can be obtained by solving equation (25) using the 4th-order Runge–Kutta method. As the damping coefficient (c) varies, the TAV changes accordingly. To determine a suitable range for the damping coefficient [$c_{\min}, c_{\max}$], $M_{L\min}$ and $M_{L\max}$ are substituted into equation (25) while considering the constraints of [$\omega'_{\min}$, $\omega'_{\max}$]. However, it is worth noting that employing the 4th-order Runge–Kutta method can be time-consuming, and it requires human intervention to select the desired damping coefficient range. Consequently, in this research, an approximate analytical solution for the TAV is derived to mitigate these challenges.

3.2. Approximate Solution of TAV. The eigenvalue equation of (12) can be written as

$$\lambda^2 + \frac{c}{I}\lambda - \frac{h}{I} = 0. \quad (15)$$

The solution of (15) can be given as

$$\lambda_{1,2} = \frac{-c/I \pm \sqrt{(c/I)^2 + 4h/I}}{2}. \quad (16)$$

As h is larger than 0, there are two unequal real roots. Then, (12) has the following general solution form:

$$\theta = A_1 e^{\lambda_1 t} + A_2 e^{\lambda_2 t}. \quad (17)$$

Meanwhile, the angular velocity can be obtained from the following equation:

$$\dot{\theta} = A_1 \lambda_1 e^{\lambda_1 t} + A_2 \lambda_2 e^{\lambda_2 t}. \quad (18)$$

By substituting (14) into (17) and (18), one can obtain

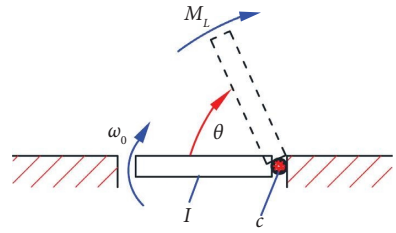

Figure 8: Dynamic model of a rotating body.

$$\begin{cases} A_1 = \dfrac{\omega_0}{\sqrt{(c/I)^2 + 4h/I}}, \\ A_2 = -\dfrac{\omega_0}{\sqrt{(c/I)^2 + 4h/I}}. \end{cases} \tag{19}$$

Then, based on (16) and (17), the analytical solutions of the angular displacement, velocity, and acceleration can be calculated as

$$\theta = \frac{\omega_0}{\sqrt{(c/I)^2 + 4h/I}}\left(e^{\lambda_1 t} - e^{\lambda_2 t}\right), \tag{20}$$

$$\dot{\theta} = \frac{\omega_0}{\sqrt{(c/I)^2 + 4h/I}}\left(\lambda_1 e^{\lambda_1 t} - \lambda_2 e^{\lambda_2 t}\right), \tag{21}$$

$$\ddot{\theta} = \frac{\omega_0}{\sqrt{(c/I)^2 + 4h/I}}\left(\lambda_1^2 e^{\lambda_1 t} - \lambda_2^2 e^{\lambda_2 t}\right). \tag{22}$$

According to (20) and (21), the relationship between angular displacement and velocity is given as

$$\frac{\dot{\theta}}{\theta} = \frac{\lambda_1 e^{\lambda_1 t} - \lambda_2 e^{\lambda_2 t}}{e^{\lambda_1 t} - e^{\lambda_2 t}}. \tag{23}$$

Moreover, it can be seen from (16) that the two characteristic roots are constant and only related to the moment of inerter I, torsional damping coefficient c, and load proportional coefficient h. Considering that λ_2 is less than zero, it is known that with the increase of time t, $e^{\lambda_2 t}$ tends to be close to zero. Thus, (23) could be simplified as

$$\frac{\dot{\theta}}{\theta} \approx \lambda_1. \tag{24}$$

Assuming that the angular displacement reaches 90° at time t_e, with the combination of (24), the TAV can be approximately determined by the following formula:

$$\dot{\theta}(t_e) \approx \lambda_1 \frac{\pi}{2} = \frac{\pi}{2} \times \left(-\frac{c}{I} + \sqrt{\left(\frac{c}{I}\right)^2 + \frac{4h}{I}}\right). \tag{25}$$

From equation (25), it is apparent that the TAV remains unaffected by the initial angular velocity ω_0. Additionally, as the torsional damping coefficient increases, the TAV experiences a reduction. The primary objective of calculating the TAV is to determine the necessary range of the damping coefficient in the subsequent section.

4. Design of the Enhanced Torsional Eddy Current Damper (ETECD)

4.1. Derivation of the Required Range of Torsional Damping Coefficient. As mentioned before, the TAV can be calculated according to equation (25). Then, based on the preset values of $\omega'_{\min}$ and $\omega'_{\max}$, the following condition should be satisfied:

$$\begin{cases} \omega'_{\min} \le \dfrac{\pi}{2} \times \left(-\dfrac{c}{I} + \sqrt{\left(\dfrac{c}{I}\right)^2 + \dfrac{4h_{\min}}{I}}\right), \\ \omega'_{\max} \ge \dfrac{\pi}{2} \times \left(-\dfrac{c}{I} + \sqrt{\left(\dfrac{c}{I}\right)^2 + \dfrac{4h_{\max}}{I}}\right), \end{cases} \tag{26}$$

where $h_{\min} = M_{L\min}/\theta, h_{\max} = M_{L\max}/\theta$. $M_{L\min}$ and $M_{L\max}$ are the minimum and maximum external torque mentioned before, respectively.

Based on (26), the torsional damping coefficient c should meet the following requirement:

$$\frac{0.5h_{\max}\pi^2 - 2I\left(\omega'_{\max}\right)^2}{\pi\omega'_{\max}} = c_{\min} \le c \le c_{\max} = \frac{0.5h_{\min}\pi^2 - 2I\left(\omega'_{\min}\right)^2}{\pi\omega'_{\min}}. \tag{27}$$

Equation (27) provides a convenient means of designing the desired range of the damping coefficient for the torsional damper under various loading conditions and velocity restrictions. The precise values of $\omega'_{\min}$, $\omega'_{\max}$, $h_{\min}$, and $h_{\max}$ are determined based on specific practical application cases.

4.2. Numerical Validation and Detailed Design Procedures of an ETECD. In this section, a numerical example is provided to validate the accuracy of (25) and the design formula equation (27). The following assumptions are made: the moment of inerter (I) is 5 kg·m^2, the initial angular velocity

(ω_0) is 1 rad/s, and the minimum and maximum external torque ($M_{L\min}$ and $M_{L\max}$) are 100θ and 500θ, respectively. The minimum and maximum TAV ($\omega'_{\min}$ and $\omega'_{\max}$) are set as 2 rad/s and 10 rad/s, respectively. Additionally, the required damping coefficient is computed using the 4th-order Runge–Kutta method with a time interval of 1×10^{-4} s, and the increment of the damping coefficient during computation is set at 0.1 N·m·s/rad.

Figure 9 illustrates the relationship between the damping coefficient of the torsional damper and the TAV obtained through the 4th-order Runge–Kutta method. Additionally, the results of TAV calculated using (25) are displayed in Figure 9. A high level of agreement is observed between the two. Besides, it can be noted that the TAV decreases with an increase in the torsional damping coefficient. From Figure 9, the required range of the damping coefficient determined through simulations is found to be from $c_{\min} = 46.80$ N·m·s/rad to $c_{\max} = 72.10$ N·m·s/rad. Similarly, the required range of the damping coefficient can be determined using (27) as 46.71 N·m·s/rad $\le c \le$ 72.17 N·m·s/rad. The damping coefficient obtained from Figure 9 closely aligns with the range determined by (27).

To validate the effectiveness of the proposed design method in controlling the rotation of the rotating body under arbitrary torques within the load range of $[M_{L\min}, M_{L\max}]$, a random torque $M_{L\text{rand}}$ is employed according to the following equation:

$$M_L = M_{L\text{rand}} = \left[h_{\min} + \left(h_{\max} - h_{\min}\right) \cdot \text{rand}\left(\right)\right] \cdot \theta, \quad (28)$$

where rand() represents a random value within the range of 0 to 1. Figure 10(a) illustrates several arbitrary load cases derived from (28). By averaging the lower and upper boundaries of the specified range, a torsional damping coefficient of $c = 59.44$ N·m·s/rad is selected. The TAV under a random load case can be calculated using (25). Figure 10(b) displays the TAV for fifty different random torsional torques $M_{L\text{rand}}$.

The observation from Figure 10(b) leads to the conclusion that, with the selected damping coefficient, the TAV conforms to the velocity restriction ($\omega'_{\min} = 2$ rad/s, $\omega'_{\max} = 10$ rad/s). Considering on the details outlined in Section 2, Section 3, and the aforementioned results, a comprehensive design procedure for the ETECD, comprising ECDs and a gearbox, is shown in Figure 11.

5. Design and Experimental Validation of an ETECD

To validate the effectiveness of the proposed design method and assess the control performance of the novel enhanced torsional eddy current damper (ETECD), a rigid rotating body was manufactured and installed in the Vibration and Shock Technology Research Center at Hunan University. The experimental setup is depicted in Figure 12, and the parameters of the rotating body are detailed in Table 1. Notably, it is assumed that the loading range and the restriction on the terminal angular velocity (TAV) have been

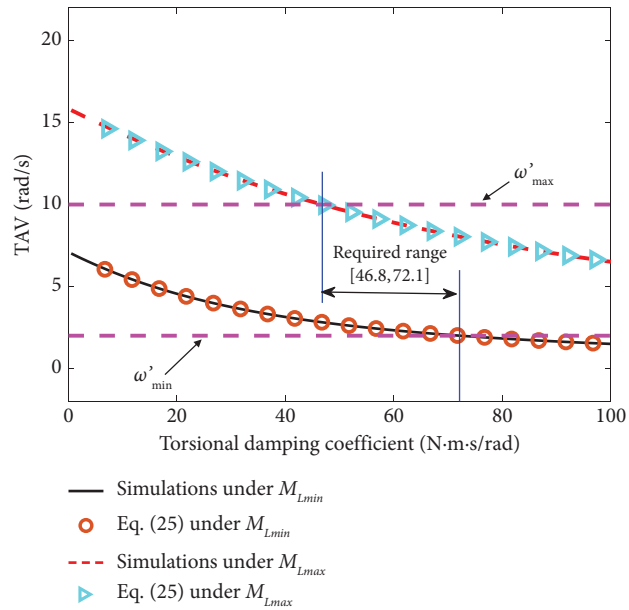

Figure 9: Variation of the TAV with damping coefficient c under ultimate torques.

assumed to be ($M_{L\min} = 165.5{\cdot}\theta$, $M_{L\max} = 636.5{\cdot}\theta$) and ($\omega'_{\min} = 3$ rad/s, $\omega'_{\max} = 13$ rad/s), respectively.

5.1. Detailed Design of the ETECD. Due to the constrained installation space of 220 mm × 90 mm × 90 mm, the torsional ECD is configured with an outer diameter (D) of 80 mm and a length (L) of 220 mm. The design includes 10 permanent magnets (PMs) with parameters: a thickness (t_m) of 10 mm, a residual magnetic field strength (B_{re}) of 1.4 T, and a relative permeability (μ_{rm}) of 1.04. The conductor tube, composed of copper, possesses a thickness (t_c) of 2 mm and a conductivity of 5.8×107 s/m. The magnetic tube thickness (t_b) is set at 5 mm, and the air gap measures 1 mm. According to equation (8), a single cylindrical ECD can provide a maximum damping coefficient of 2.37 N·m·s/rad. By substituting this damping coefficient into equation (25), the terminal angular velocity (TAV) under the maximum torsional torque $M_{L\max} = 636.5{\cdot}\theta$ is calculated to be 54.21 rad/s, overtaking the maximum velocity restriction of 13 rad/s. Consequently, the ETECD becomes necessary.

According to the spatial relationship between the installation positions of the rotating body and the damper, the damper is configured as two cylindrical torsional ECDs, symmetrically positioned on both sides of the gearbox, as illustrated in Figure 13(a). The ETECD comprises two cylindrical torsional ECDs, each with a length (L) of 60 mm. The length of the gearbox and other parts totals 100 mm, as shown in Figure 13(b). Each ECD is equipped with 8 PMs, with a distance (d_m) between each PM as 9.42 mm. The dimensional parameters of the cylindrical ECD are outlined in Table 2. With the specified parameters, the total damping coefficient of these two torsional ECDs amounts to 0.997 N·m·s/rad.

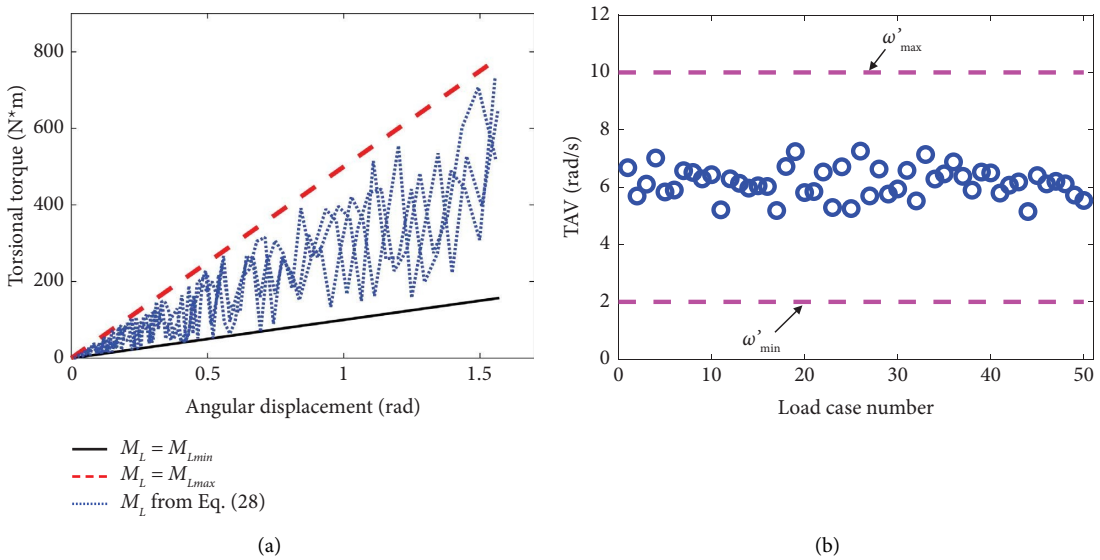

FIGURE 10: Response of rotating body under different external torsional torques. (a) Torsional torque-rotation angle. (b) TAV under random torque.

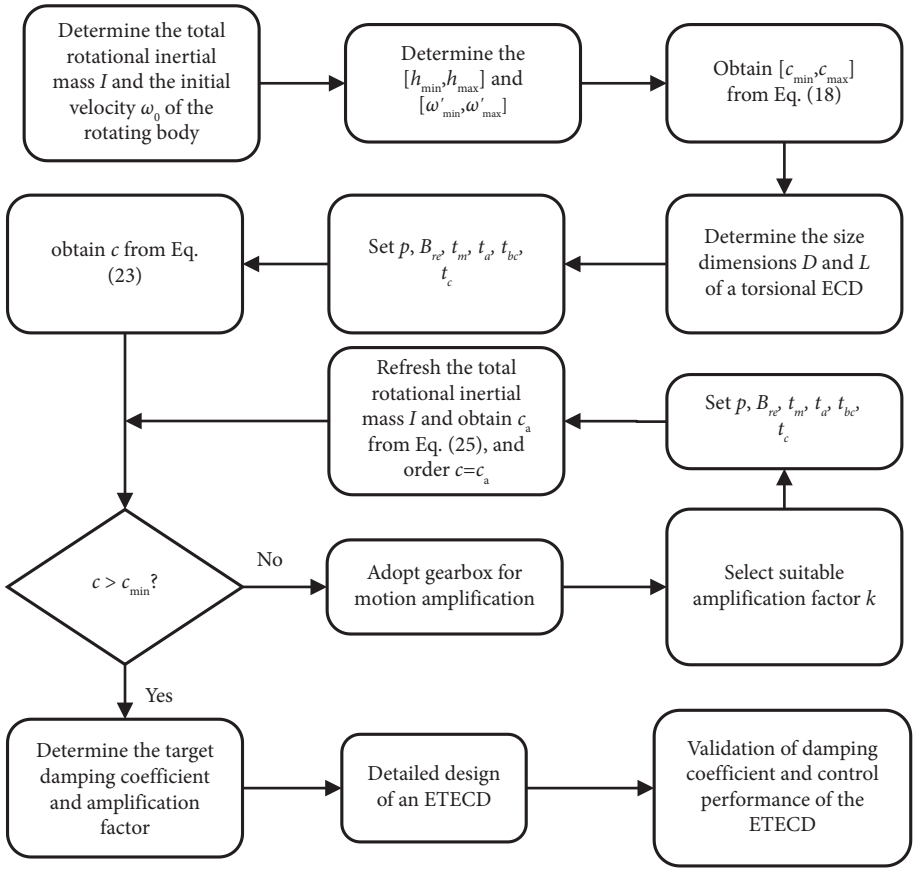

FIGURE 11: The design procedures of an ETECD for a rotating body.

For precise determination of the amplification factor k, a three-dimensional finite element model (3D FEM) of the cylindrical ECD is constructed to compute its damping coefficient. The 3D FEM accounts for axial, radial, and circumferential magnetic field distributions. Hexahedral elements are utilized for modeling the permanent magnet (PM), air gap, conductor, back iron of PM, and back iron of conductor in the model. This ensures accurate computation

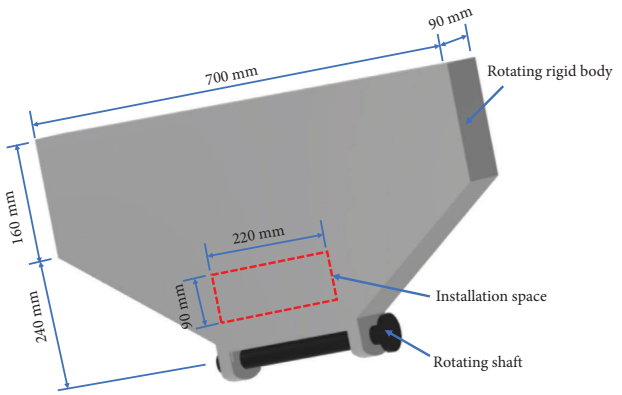

Figure 12: Dimensions and detailed parameters of the rotating body.

Table 1: Parameters of the rotating body.

Parameter	Symbol	Value	Unit
Initial velocity	ω_0	0	rad/s
Mass	m_0	30	kg
Rotation angle	θ	From 0 to 90	°
Moment of inerter	I	2	kg·m^2
External torsional torque	M_L	$165.5{\cdot}\theta \le M_L \le 636.5{\cdot}\theta$	N·m

of damping torque with varying rotation velocities, which was validated by Zhang et al. [50]. Considering that adjacent PMs within one revolution have identical dimensions and opposite magnetization, the damper can be simplified for computation using a $1/2p$ three-dimensional finite element model through antisymmetric periodic conditions. The periodic conditions and meshing of the model in this research are illustrated in Figure 14.

Figure 15(a) depicts the eddy current density distribution in the three-dimensional model, while Figure 15(b) illustrates the relationship between the damping torque and the angular velocity. It is evident from Figure 15(b) that the damping torque demonstrates a linear relationship with the angular velocity within the range of 0 to 110 rad/s. Furthermore, the average damping coefficient within this velocity range is calculated as $c = 1.007$ N·m·s/rad, which closely aligns with the estimated value of 0.997 N·m·s/rad.

Utilizing (27), the required range of the damping coefficient is determined to be between 60.36 N·m·s/rad and 82.84 N·m·s/rad. For the design target, the damping coefficient is set as $c = (60.36 + 82.84)/2 = 71.60$ N·m·s/rad. Referring to (8) and considering the aforementioned damping coefficient of the cylindrical ECD, the required amplification factor for the gearbox is determined as $k = 8.43$. Consequently, the gearbox is designed with four gears, as depicted in Figure 7. The number of teeth for these gears is specified as $Z1 = 41$, $Z2 = 16$, $Z3 = 65$, and $Z4 = 20$, respectively. According to (10), the amplification factor of the gearbox is calculated to be 8.33, which is close to the required value.

The damping coefficient obtained from equation (9) and 3D FEM of the damper are 69.18 N·m·s/rad and 69.87 N·m·s/rad, respectively, meeting the control requirements. Considering that the amplification factor $k = 8.33$ and the damping coefficient of the ECD without amplification gears is 0.997 N·m·s/rad, the enhanced damping coefficient of the proposed ETECD is $c_a = k^2 \times c = 69.18$ N·m·s/rad.

The mass and equivalent rotational inertial masses of the amplified parts of the ETECD (PMs, gears, their shaft, and back iron of PMs) are provided in Table 3. As shown in Table 3, the equivalent inertial mass of the amplified parts of the ETECD is relatively small, and the total equivalent rotational inertial mass of them is 0.029 kg·m^2. Meanwhile, the rotational inertial mass of the rotating body is 2 kg·m^2, and the amplified parts of the ETECD may exert limited influence on the results.

5.2. Experimental Measurement of the Damping Coefficient of ETECD. Following the aforementioned design procedure, an ETECD has been manufactured, comprising two torsional cylindrical ECDs and a gearbox, as depicted in Figure 16. For experimental purposes, the corresponding setup is illustrated in Figure 17. The rotational component, coupled with the ETECD, is fastened and connected to the base. To apply variable angular velocities, a rotary drive mechanism is attached to the rotational shaft of the rigid body.

For quantifying the damping torque and angular displacement of the ETECD, a torque sensor and an angular displacement sensor have been positioned on the shaft. Both sensors operate at a sampling frequency of 2 kHz. The angular velocity can be derived from the time derivative of the angular displacement history.

The damping torque measured by the ETECD under various angular velocities is shown in Figure 18. Additionally, the estimated values from (9) and results obtained from the 3D FEM analysis are plotted in Figure 18 for comparison. The average torsional damping coefficient from experimental results is calculated as $c = 70.04$ N·m·s/rad, which is very close to the required torsional damping coefficient of 71.60 N·m·s/rad and the designed torsional damping coefficient (3D FEM) of 69.87 N·m·s/rad.

Furthermore, the experimentally measured damping coefficient is larger than both the FEM (69.87 N·m·s/rad) and estimated results (69.18 N·m·s/rad). This difference may be attributed to minor manufacturing errors and incomplete uniform magnetization of the permanent magnets. Nevertheless, this difference does not impact the final control performance. Therefore, the manufactured ETECD can be directly utilized for the control of the rotating body.

5.3. Comparison with Axial ECD. For the purpose of comparing the enhanced torsional eddy current damper (ETECD) presented in this research with the axial eddy current damper (ECD), a rack is installed next to Gear 1 in this section. It is assumed that the length of the rack is equal to the circumference of Gear 1, and the rack has the same module and tooth size as Gear 1. As shown in Figure 7, the diameter of Gear 1 is 75.25 mm and the circumference is 236.29 mm. Assuming that the axial movement velocity of the rack is 236.29 mm/s (corresponding to a rotation

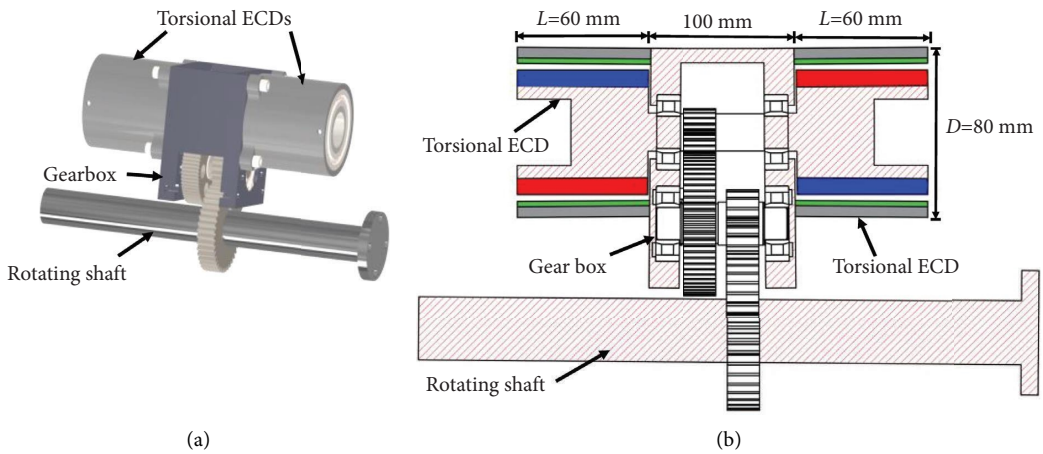

Figure 13: The enhanced torsional eddy current damper (ETECD). (a) 3D layout diagram. (b) Detailed configuration.

Table 2: Parameters of the cylindrical ECD (unit: mm).

Parameters	Symbol	Value
The outer radius of the damper	R_o	40
The outer radius of the conductor	R_b	35
The internal radius of the conductor	R_c	33
The outer radius of PMs	R_m	32
The internal radius of PMs	R_d	22

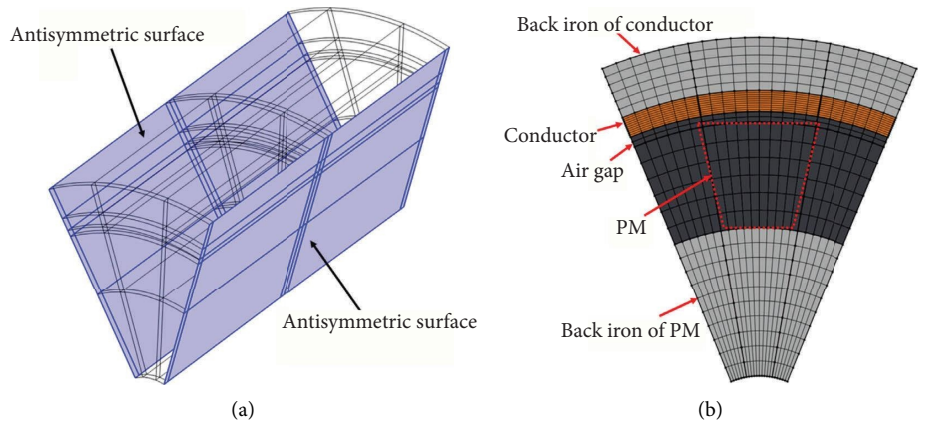

Figure 14: 1/2p three-dimensional finite element model. (a) Model with antisymmetric periodic conditions. (b) Meshing.

velocities of 6.28 rad/s for Gear 1), the relative velocity between the permanent magnets and the conductor in the axial eddy current damper without motion-amplified device is 236.29 mm/s. However, after the installation of motion-amplified device, the relative rotational velocity between the permanent magnets (PMs) and the conductor is 53.31 rad/s ($6.28 \times 8.33 = 53.31$ rad/s), and the corresponding relative velocity between them is 1702.72 mm/s. At this point, the relative velocity has increased by approximately 7.21 times. As the damping force is approximately linearly related to speed at low speeds, this implies that the damping coefficient has increased by about 51.93 times. For a sinusoidal displacement loading motion with a displacement of 100 mm and a frequency of 1 Hz, the force-displacement curves of the two dampers with the same specifications and dimensions are shown in Figure 19, and the damping coefficients of the two dampers are 0.22 N·s/mm and 11.55 N·s/mm, respectively. It can be calculated from Figure 19 that the energy consumption from the proposed ETECD under a sinusoidal displacement loading is 2278 J, which is almost 52.50 times to the axial ECD.

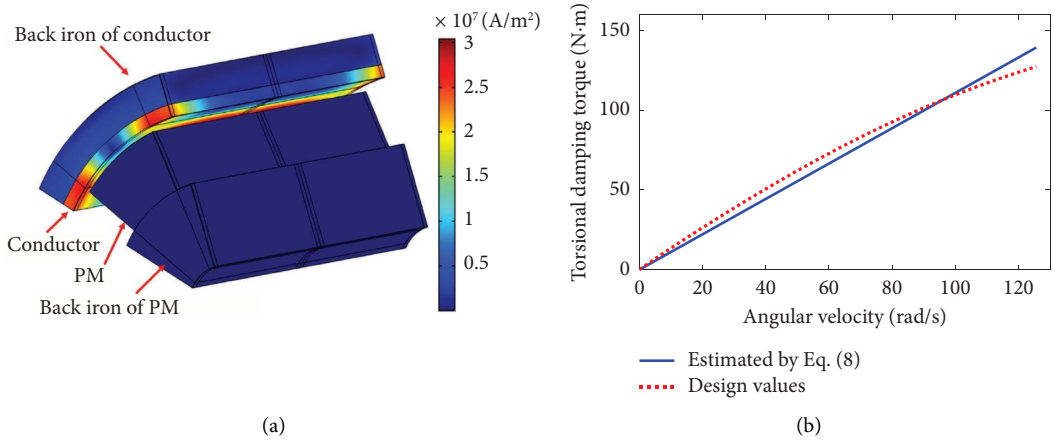

Figure 15: Finite element model of the torsional ECD. (a) Eddy current density distribution. (b) Damping torque-angular velocity.

Table 3: Mass and equivalent inertial mass of gear, PMs, and back iron of PMs.

Components	Mass (kg)	Rotational inertial mass (kg·mm^2)	Motion amplification factor	Equivalent rotational inertial mass (kg·m^2)
Gear 2 and 3 and their shaft (I_{g23})	0.43	176.69	2.56	0.0012
Gear 4 and its shaft (I_{g4})	0.20	6.63	8.33	0.0005
Back iron of PMs (I_{bm})	1.01	139.43	8.33	0.0097
PMs (I_m)	0.33	255.70	8.33	0.0177

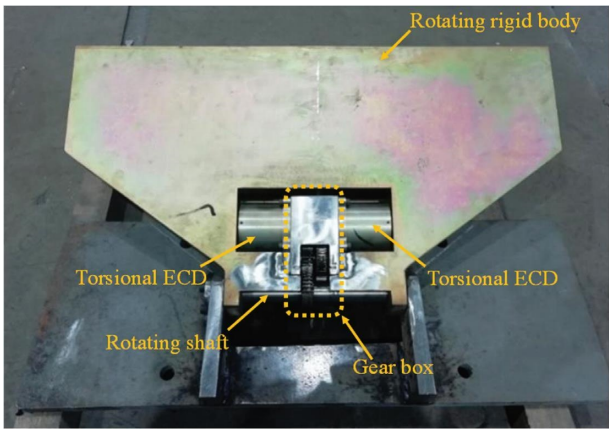

Figure 16: Photo of the rotating body with ETECD.

5.4. Validation of Control Performance. In this section, the control performance of the manufactured ETECD is verified by subjecting the rotating body to both maximum and minimum external torsional torques.

5.4.1. Measured Results under Minimum External Torsional Torque MLmin. For the minimum loading case, dropping a heavy mass is used to drive the rotating body to produce the rotational motion. The experimental configuration of the weight-loading system is depicted in Figure 20. In this setup, the rotating body is linked to the mass m_1 via a steel cable passing through a fixed pulley, while the rotating shaft is fixed to the ground. A buffering block is installed to mitigate shock effects from high TAV. An electromagnet on the ground secures the rotating body when activated. An angular displacement sensor is positioned on the rotating shaft for measuring angular displacement, and a load sensor on the cable measures the tension force F_s in the connection cable. Both the load sensor and angular displacement sensor operate at a sampling frequency of 2 kH.

Utilizing the weight-loading system, the performance of the ETECD under the minimum loading case is investigated. In Figure 21(a), the "Targeted value" represents theoretical values of the external torque (M_{Lmin}) changed with the angular displacement, and the "Measured value" corresponds to the external torque applied to the rotating body. Figure 21(a) illustrates the measured torque on the rotating body compared with the targeted value. The relation between angular displacement and velocity of the rotating body, with and without control, is also compared in Figure 21(b). In Figure 21(b), "Uncontrolled (Num.)" represents numerical simulations for the uncontrolled state. "Controlled (Num. ES)" corresponds to numerical simulations for the controlled state, considering the total rotational inertial mass of the entire system. "Controlled (Num. RB)" corresponds to numerical simulations for the controlled state, considering the rotational inertial mass of the rotating body only. "Controlled (Exp.)" represents the controlled state with experimental measurements. All these depict the variation of velocity with angle. It can be found from Figure 21(a) that the experimentally applied torque is slightly higher than the targeted value due to neglecting the weight of the load sensor and other connected parts. This causes that the angular velocity in the experiment is larger than the simulation results during the loading process. Moreover, fluctuations in the measured loading curve caused by the

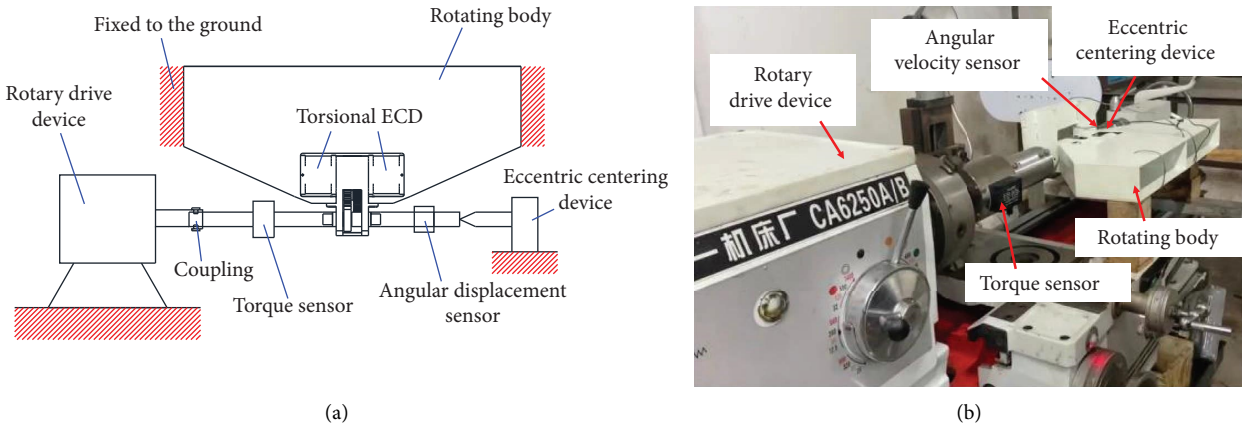

FIGURE 17: Measurement of the torsional damping coefficient. (a) Schematic diagram. (b) Setup of measurement.

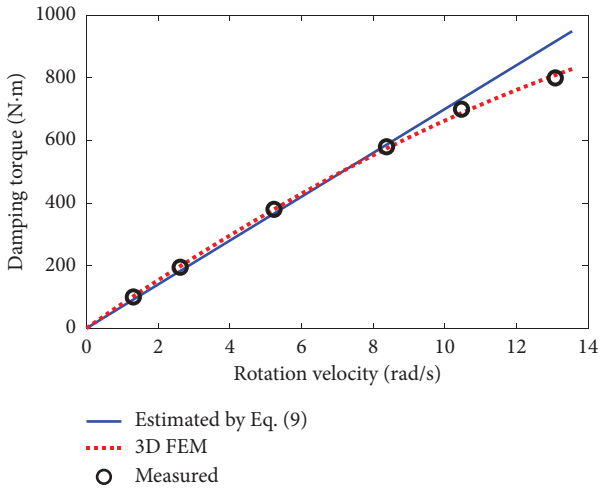

FIGURE 18: Damping coefficient of the ETECD.

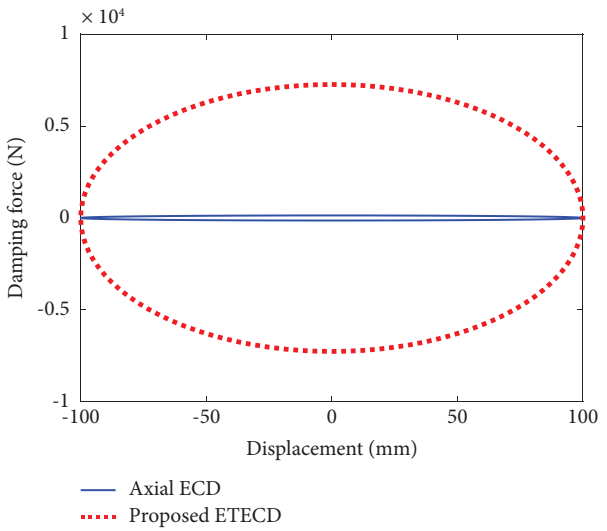

FIGURE 19: The force-displacement curves of the two dampers.

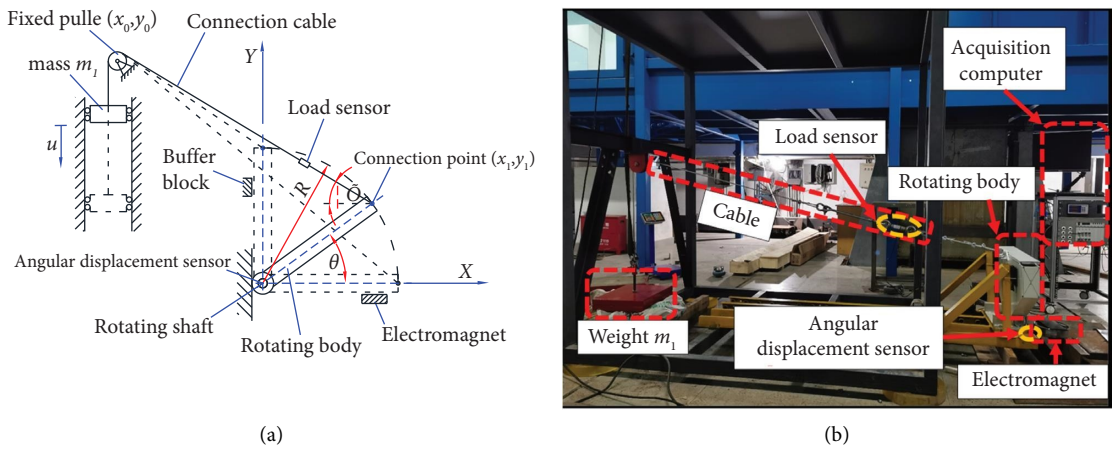

FIGURE 20: Schematic diagram and experimental of the weight-loading system. (a) Schematic diagram. (b) Experimental setup.

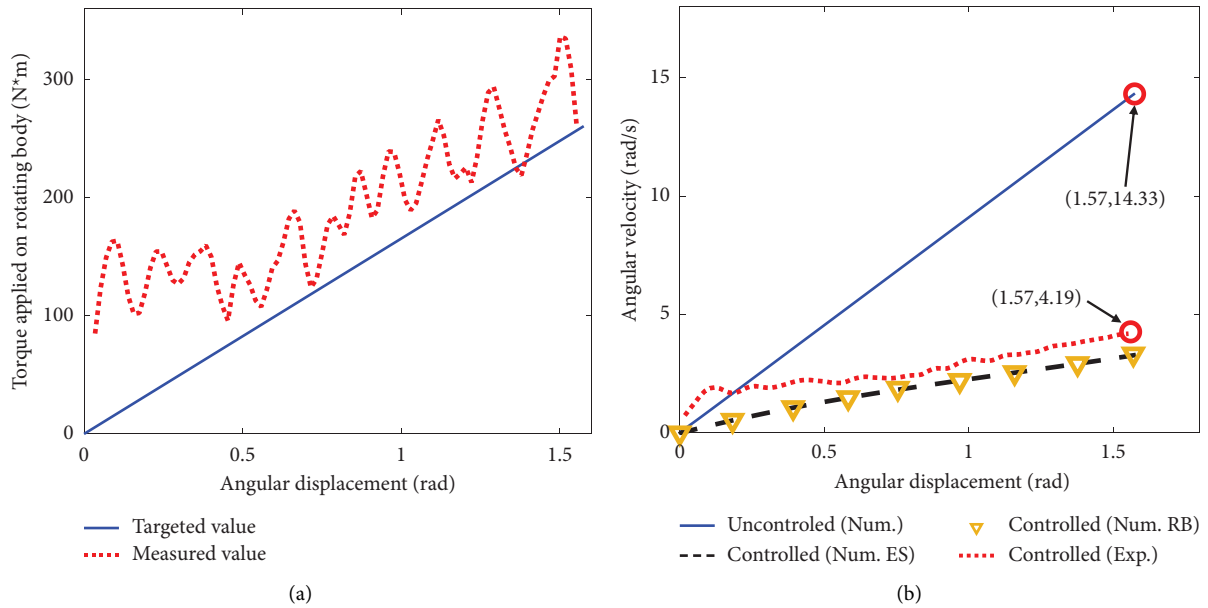

FIGURE 21: Comparison of uncontrolled and controlled value under $M_{L\min}$. (a) Torque-angular displacement. (b) Angular velocity-displacement.

vibration of the connection cable during the rotation process can be observed. In Figure 21(b), the experimental results of angular velocity show a nearly linearly proportional to the displacement, verifying the reliability of the analytical relation as expressed by (24). Additionally, with and without the equivalent rotational inertial mass of the amplified parts of the ETECD, the angular velocities obtained from numerical simulation agree well with each other. The influence of the equivalent inertial mass of the amplified parts of the ETECD in the loading case of $M_{L\min}$ can be negligible. Moreover, with the installation of the proposed ETECD, the TAV reduces from 14.33 to 4.19 rad/s, signifying the capability of the proposed ETECD to effectively control the rotating body in the loading case of $M_{L\min}$.

5.4.2. Measured Results under Maximum External Torsional Torque $M_{L\max}$. In this case, a hydraulic loading system is employed instead of a weight-loading system to generate the maximum loading case. The experimental setup is depicted in Figure 22. The rotating body is linked to the actuator of the hydraulic loading actuator via a steel rod, while the rotating shaft is fixed to the ground. A buffering block is utilized to prevent the shocking failure arising from high terminal angular velocity (TAV). An angular displacement sensor is positioned on the rotating shaft for measuring the angular displacement, and a load sensor is placed on the steel rod to measure the tension force F_s in the steel rod. The sampling frequency is set to 2 kHz.

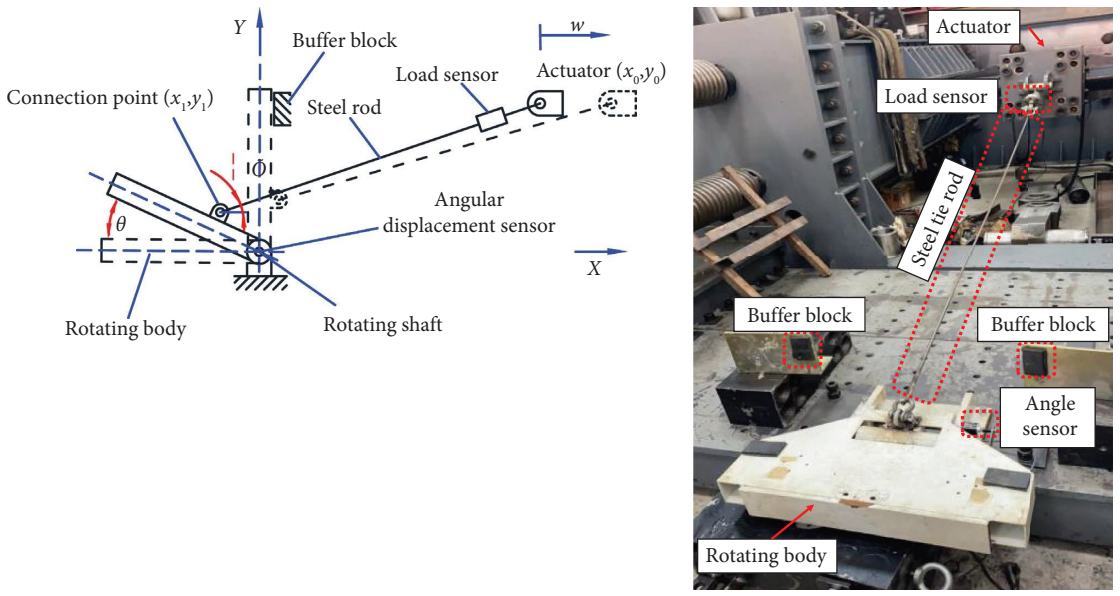

(a) (b)

FIGURE 22: Schematic diagram and experiment of hydraulic loading system. (a) Schematic diagram. (b) Experimental setup.

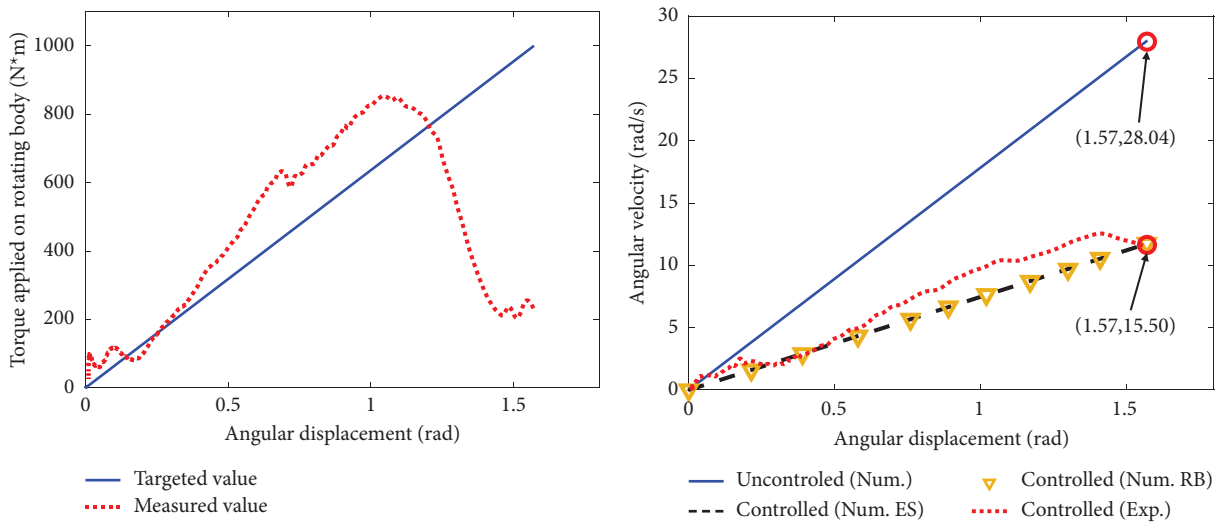

(a) (b)

FIGURE 23: Comparison of uncontrolled and controlled values under M_{Lmax}. (a) Torque-angular displacement. (b) Angular velocity-displacement.

The legend in Figure 23 has the same meaning as in Figure 21. The output loading curve generated by the actuator is plotted in Figure 23(a). The corresponding targeted value is also presented in Figure 23(a) for comparison. The generated external torque at the beginning of loading process is lightly larger than the target value, and the generated external torque decreases significantly at the end of the loading process. This is because that the hydraulic pump will be cut off in advance to ensure the safety of the actuator device. However, for accurately simulating the maximum loading case, the input energy applied to the rotating body by the actuator during the loading process will be set to identical to the maximum loading case.

Based on the area enveloped by the torque and angular displacement curve in Figure 23(a), the input energy applied to the rotating body by the actuator is calculated as 790.05 J, which aligns well with the target curve's energy of 785.50 J. Moreover, Figure 23(b) displays the experimental curve of angular velocity and displacement. The TAV is reduced from 28.04 rad/s to 11.50 rad/s after installing the proposed ETECD. Additionally, considering and not considering the equivalent rotational inertial mass of the amplified parts of the ETECD, the angular

velocities agree well with each other, which means that the influence of the equivalent rotational inertial mass of the amplified parts of the ETECD in this work can be negligible. However, it is essential to note that careful consideration is needed when the equivalent inertial mass of the damper is relatively large compared to that of the rotating body. As seen in Figure 23(b), the measured angular velocity is slightly larger than the numerical simulation results during the loading process. This is mainly because the torque applied on the rotating body from the actuator is larger than the targeted value at the beginning stage. However, the error in testing energy input does not affect the generality of the conclusions. It can be inferred that for both minimum and maximum loading cases, the ETECD can effectively control the rotational motion.

6. Conclusions

This study introduces an enhanced torsional eddy current damper (ETECD), consisting of cylindrical ECDs and gearboxes, which could be used for controlling a rotating body. The damping estimation method is proposed for estimating the damping coefficient of cylindrical ECD. Before detailing the design of the proposed ETECD, this study presents the motion equation and solution of the rotating body with a torsional damper. For a rotating body requiring angular velocity control within a specified limit, while considering a particular load range during rotational motion, the required range of the torsional damping coefficient is derived.

The control effects of the ETECD are assessed both numerically and experimentally under maximum external torsional torque ($M_{L\max}$) and minimum external torsional torque ($M_{L\min}$). The results obtained from the approximate solution closely align with those obtained analytically.

By selecting a damping coefficient within the proposed range, the terminal angular velocity (TAV) meets with the angular velocity constraints even under the application of linear and random torques. The estimated value and measured value of the damping coefficient for the ETECD are 69.18 N·m·s/rad and 70.04 N·m·s/rad, respectively, validating the efficacy of the proposed damping coefficient estimation method. Experimental results indicate a substantial reduction in TAV, amounting to 70.76% and 58.99% for the $M_{L\min}$ and $M_{L\max}$ cases, respectively.

Data Availability

The data used to support the findings of this study are available from the corresponding author upon reasonable request.

Conflicts of Interest

The authors declare that they have no conflicts of interest.

Acknowledgments

This work was supported by the National Natural Science Foundation of China (grant nos. U2141242, 52278304, 51908210, 52025082, and 52208478), the Science and Technology Innovation Program of Hunan Province (grant no. 2023RC3090), the Changsha Outstanding Innovative Youth Culturing Program (grant no. kq2209009), the Natural Foundation of Hunan Province (grant no. 2020JJ5074), and the Science Research Project of Education Department at Hunan Province (grant no. 20K029).

References

[1] D. Kahveci and Y. Yaylı, "Geometric kinematics of persistent rigid motions in three-dimensional Minkowski space," *Mechanism and Machine Theory*, vol. 167, Article ID 104535, 2022.

[2] F. Hou, P. P. Sarkar, and A. Alipour, "A novel mechanism smart morphing façade system to mitigate wind-induced vibration of tall buildings," *Engineering Structures*, vol. 275, Article ID 115152, 2023.

[3] J. J. de Jong, A. Müller, and J. L. Herder, "Higher-order derivatives of rigid body dynamics with application to the dynamic balance of spatial linkages," *Mechanism and Machine Theory*, vol. 155, Article ID 104059, 2021.

[4] L. B. Saint Martin, L. L. Gusmão, T. H. Machado, E. P. Okabe, and K. L. Cavalca, "Operational modal analysis application to support structure identification under rotating machinery unbalance," *Engineering Structures*, vol. 249, Article ID 113344, 2021.

[5] C. Fan, Z. Xu, Y. Han, Y. Liu, and F. Huang, "Loading rate effect and failure mechanisms of ultra-high-strength steel under mode II fracture," *International Journal of Impact Engineering*, vol. 171, Article ID 104374, 2023.

[6] S. C. Jun, C. H. Lee, and C. J. Bae, "Shake table testing of braced and Friction-Added suspended ceilings and associated numerical study," *Engineering Structures*, vol. 252, Article ID 113724, 2022.

[7] L. Zheng, T. Yang, S. Xue, G. Li, and X. Liu, "Fracture failure analysis of the teeth of conjunction gear made of 20MnCr5S steel," *Engineering Failure Analysis*, vol. 134, Article ID 106006, 2022.

[8] Y. Liu, M. Wan, Q. B. Xiao, and W. H. Zhang, "Identification and compensation of geometric errors of rotary axes in five-axis machine tools through constructing equivalent rotary axis (ERA)," *International Journal of Mechanical Sciences*, vol. 152, pp. 211–227, 2019.

[9] S. Chapain and A. M. Aly, "Vibration attenuation in wind turbines: a proposed robust pendulum pounding TMD," *Engineering Structures*, vol. 233, Article ID 111891, 2021.

[10] A. Miyake, A. Kitakaze, S. Katoh et al., "Chip control in turning with synchronization of spindle rotation and feed motion vibration," *Precision Engineering*, vol. 53, pp. 38–45, 2018.

[11] T. Ho, K. Suzuki, M. Tsume, R. Tasaki, T. Miyoshi, and K. Terashima, "A switched optimal control approach to reduce transferring time, energy consumption, and residual vibration of payload's skew rotation in crane systems," *Control Engineering Practice*, vol. 84, pp. 247–260, 2019.

[12] S. Bai, J. Cui, Y. Zheng et al., "Electromagnetic-triboelectric energy harvester based on vibration-to-rotation conversion for human motion energy exploitation," *Applied Energy*, vol. 329, Article ID 120292, 2023.

[13] G. Yu, L. He, H. Wang, L. Sun, Z. Zhang, and G. Cheng, "Research of rotating piezoelectric energy harvester for automotive motion," *Renewable Energy*, vol. 211, pp. 484–493, 2023.

[14] J. S. Hwang, J. Kim, and Y. M. Kim, "Rotational inertia dampers with toggle bracing for vibration control of

a building structure," *Engineering Structures*, vol. 29, no. 6, pp. 1201–1208, 2007.
[15] D. B. Wang, X. Fu, and H. J. Liu, "Study on the performance of a novel rotation-amplified brace and its vibration control for a frame structure," *Structures*, vol. 57, Article ID 105142, 2023.
[16] L. Chen, L. Sun, and S. Nagarajaiah, "Cable vibration control with both lateral and rotational dampers attached at an intermediate location," *Journal of Sound and Vibration*, vol. 377, pp. 38–57, 2016.
[17] Re-entry Burns of Falcon, "The space techie," 2021, https://www.thespacetechie.com/re-entry-burns-of-falcon-9/.
[18] https://v.qq.com/x/page/a3262khnogl.html.
[19] L. Giresini, "Effect of dampers on the seismic performance of masonry walls assessed through fragility and demand hazard curves," *Engineering Structures*, vol. 261, Article ID 114295, 2022.
[20] P. Museros and M. D. Martinez-Rodrigo, "Vibration control of simply supported beams under moving loads using fluid viscous dampers," *Journal of Sound and Vibration*, vol. 300, no. 1-2, pp. 292–315, 2007.
[21] V. Jahangiri, C. Sun, and F. Kong, "Study on a 3D pounding pendulum TMD for mitigating bi-directional vibration of offshore wind turbines," *Engineering Structures*, vol. 241, Article ID 112383, 2021.
[22] Z. Shu, S. Li, J. Zhang, and M. He, "Optimum seismic design of a power plant building with pendulum tuned mass damper system by its heavy suspended buckets," *Engineering Structures*, vol. 136, pp. 114–132, 2017.
[23] S. L. Yeh and R. L. Harne, "Origins of broadband vibration attenuation empowered by optimized viscoelastic metamaterial inclusions," *Journal of Sound and Vibration*, vol. 458, pp. 218–237, 2019.
[24] C. A. F. Silva, L. Manin, R. G. Rinaldi, E. Besnier, and D. Remond, "Dynamics of Torsional Vibration Damper (TVD) pulley, implementation of a rubber elastomeric behavior, simulations and experiments," *Mechanism and Machine Theory*, vol. 142, Article ID 103583, 2019.
[25] W. Zhang, B. Han, X. Li, J. Sun, and Q. Ding, "Multiple-objective design optimization of squirrel cage for squeeze film damper by using cell mapping method and experimental validation," *Mechanism and Machine Theory*, vol. 132, pp. 66–79, 2019.
[26] X. Zhang, G. Cheng, Z. You, and H. Zhang, "Energy absorption of axially compressed thin-walled square tubes with patterns," *Thin-Walled Structures*, vol. 45, no. 9, pp. 737–746, 2007.
[27] Z. He, X. Huang, Z. D. Xu, Q. Shi, Y. Guo, and J. Kim, "Experimental study on seismic performance of prefabricated viscoelastic damping bolted joints," *Engineering Structures*, vol. 256, Article ID 113933, 2022.
[28] A. González Ureña, R. Tremblay, and C. A. Rogers, "Experimental and numerical study of square HSS BIEs under cyclic loading," *Engineering Structures*, vol. 252, Article ID 113669, 2022.
[29] A. Pall and C. Marsh, "Response of friction damped braced frames," *Journal of the Structural Division*, vol. 108, no. 6, pp. 1313–1323, 1982.
[30] I. H. Mualla and B. Belev, "Performance of steel frames with a new friction damper device under earthquake excitation," *Engineering Structures*, vol. 24, no. 3, pp. 365–371, 2002.
[31] K.-C. Tsai, H.-W. Chen, C.-P. Hong, and Y.-F. Su, "Design of steel triangular plate energy absorbers for seismic-resistant construction," *Earthquake Spectra*, vol. 9, no. 3, pp. 505–528, 1993.
[32] J. Kelly, R. Skinner, and A. Heine, "Mechanisms of energy absorption in special devices for use in earthquake resistant structures," *Engineering*, vol. 9, p. 30, 1972.
[33] A. Whittaker, V. V. Bertero, C. L. Thompson, and L. J. Alonso, "Seismic testing of steel plate energy dissipation devices," *Earthquake Spectra*, vol. 7, no. 4, pp. 563–604, 1991.
[34] G. Cheng, N. Yu, and N. Olhoff, "Optimum design of thermally loaded beam-columns for maximum vibration frequency or buckling temperature," *International Journal of Solids and Structures*, vol. 66, pp. 20–34, 2015.
[35] Y. Nie, Z. Li, and G. Cheng, "Efficient prediction of the effective nonlinear properties of porous material by FEM-Cluster based Analysis (FCA)," *Computer Methods in Applied Mechanics and Engineering*, vol. 383, Article ID 113921, 2021.
[36] A. Pazooki, A. Goodarzi, A. Khajepour, A. Soltani, and C. Porlier, "A novel approach for the design and analysis of nonlinear dampers for automotive suspensions," *Journal of Vibration and Control*, vol. 24, no. 14, pp. 3132–3147, 2018.
[37] B. G. Kim, D. S. Yoon, G. W. Kim, S. B. Choi, A. S. Tan, and T. Sattel, "Design of a novel magnetorheological damper adaptable to low and high stroke velocity of vehicle suspension system," *Applied Sciences*, vol. 10, no. 16, p. 5586, 2020.
[38] J. D. Kang and Y. Mori, "Simplified estimation method of inelastic seismic demands of buildings with seesaw system using fluid viscous dampers," *Engineering Structures*, vol. 138, pp. 120–130, 2017.
[39] G. M. Del Gobbo, M. S. Williams, and A. Blakeborough, "Comparing fluid viscous damper placement methods considering total-building seismic performance," *Earthquake Engineering & Structural Dynamics*, vol. 47, no. 14, pp. 2864–2886, 2018.
[40] J. Chen, X. Zeng, and Y. Peng, "Probabilistic analysis of wind-induced vibration mitigation of structures by fluid viscous dampers," *Journal of Sound and Vibration*, vol. 409, pp. 287–305, 2017.
[41] G. Maddaloni, N. Caterino, and A. Occhiuzzi, "Shake table investigation of a structure isolated by recycled rubber devices and magnetorheological dampers: hybrid Isolation," *Structural Control and Health Monitoring*, vol. 24, no. 5, Article ID e1906, 2017.
[42] H. A. Sodano and D. J. Inman, "Non-contact vibration control system employing an active eddy current damper," *Journal of Sound and Vibration*, vol. 305, no. 4-5, pp. 596–613, 2007.
[43] R. Jeyasenthil and S. B. Choi, "A novel semi-active control strategy based on the quantitative feedback theory for a vehicle suspension system with magneto-rheological damper saturation," *Mechatronics*, vol. 54, pp. 36–51, 2018.
[44] P. Zhou, M. Liu, W. Kong, Y. Xu, and H. Li, "Modeling and evaluation of magnetorheological dampers with fluid leakage for cable vibration control," *Journal of Bridge Engineering*, vol. 26, no. 2, Article ID 04020119, 2021.
[45] H. Wang, H. Gao, J. Li, Z. Wang, Y. Ni, and R. Liang, "Optimum design and performance evaluation of the tuned inerter-negative-stiffness damper for seismic protection of single-degree-of-freedom structures," *International Journal of Mechanical Sciences*, vol. 212, Article ID 106805, 2021.
[46] J. S. Bae, M. K. Kwak, and D. J. Inman, "Vibration suppression of a cantilever beam using eddy current damper," *Journal of Sound and Vibration*, vol. 284, no. 3-5, pp. 805–824, 2005.
[47] J. G. Detoni, Q. Cui, N. Amati, and A. Tonoli, "Modeling and evaluation of damping coefficient of eddy current dampers in

rotordynamic applications," *Journal of Sound and Vibration*, vol. 373, pp. 52–65, 2016.

[48] D. Saige, J. Engelhardt, and S. Katz, "Application of eddy current damper technology for passive tuned mass damper systems within footbridges," *Procedia Engineering*, vol. 199, pp. 1804–1809, 2017.

[49] M. Amjadian and A. K. Agrawal, "Modeling, design, and testing of a proof-of-concept prototype damper with friction and eddy current damping effects," *Journal of Sound and Vibration*, vol. 413, pp. 225–249, 2018.

[50] H. Y. Zhang, Z. Q. Chen, X. G. Hua, Z. W. Huang, and H. W. Niu, "Design and dynamic characterization of a large-scale eddy current damper with enhanced performance for vibration control," *Mechanical Systems and Signal Processing*, vol. 145, Article ID 106879, 2020.

[51] S. Liu, Z. Lu, P. Li, S. Ding, and F. Wan, "Shaking table test and numerical simulation of eddy-current tuned mass damper for structural seismic control considering soil-structure interaction," *Engineering Structures*, vol. 212, Article ID 110531, 2020.

[52] J. S. Bae, M. K. Kwak, and D. J. Inman, "Vibration suppression of a cantilever beam using eddy current damper," *Journal of Sound and Vibration*, vol. 284, no. 3–5, pp. 805–824, 2005.

[53] Y. Liu, K. Wang, O. Mercan, H. Chen, and P. Tan, "Experimental and numerical studies on the optimal design of tuned mass dampers for vibration control of high-rise structures," *Engineering Structures*, vol. 211, Article ID 110486, 2020.

[54] A. Asghar Maddah, Y. Hojjat, M. Reza Karafi, and M. Reza Ashory, "Reduction of magneto rheological dampers stiffness by incorporating of an eddy current damper," *Journal of Sound and Vibration*, vol. 396, pp. 51–68, 2017.

[55] L. Irazu and M. J. Elejabarrieta, "Analysis and numerical modelling of eddy current damper for vibration problems," *Journal of Sound and Vibration*, vol. 426, pp. 75–89, 2018.

[56] Z. Lu, B. Huang, Q. Zhang, and X. Lu, "Experimental and analytical study on vibration control effects of eddy-current tuned mass dampers under seismic excitations," *Journal of Sound and Vibration*, vol. 421, pp. 153–165, 2018.

[57] W. Yang, H. Zhang, Z. Chen, X. Hua, H. Niu, and S. Li, "Study on enhanced performance of CuFe alloy's eddy current damping and its advantages in multi-mode vibration control of stay-cable," *Engineering Structures*, vol. 299, Article ID 117102, 2024.

[58] S. Kawamata, M. Yoneda, and Y. Hangai, *Development of Vibration Control System for Structures by Means of Mass Pumps*, University of Tokyo, Tokyo, Japan, 1973.

[59] M. C. Smith, "Synthesis of mechanical networks: the inerter," *IEEE Transactions on Automatic Control*, vol. 47, no. 10, pp. 1648–1662, 2002.

[60] Z. Zhao, Q. Chen, R. Zhang, C. Pan, and Y. Jiang, "Energy dissipation mechanism of inerter systems," *International Journal of Mechanical Sciences*, vol. 184, Article ID 105845, 2020.

[61] D. J. Wagg, "A review of the mechanical inerter: historical context, physical realisations and nonlinear applications," *Nonlinear Dynamics*, vol. 104, no. 1, pp. 13–34, 2021.

[62] Q. Chen, Z. Zhao, Y. Xia, C. Pan, H. Luo, and R. Zhang, "Comfort based floor design employing tuned inerter mass system," *Journal of Sound and Vibration*, vol. 458, pp. 143–157, 2019.

[63] D. De Domenico, P. Deastra, G. Ricciardi, N. D. Sims, and D. J. Wagg, "Novel fluid inerter based tuned mass dampers for optimised structural control of base-isolated buildings," *Journal of the Franklin Institute*, vol. 356, no. 14, pp. 7626–7649, 2019.

[64] I. F. Lazar, S. A. Neild, and D. J. Wagg, "Vibration suppression of cables using tuned inerter dampers," *Engineering Structures*, vol. 122, pp. 62–71, 2016.

[65] A. D. Shaw, S. A. Neild, and D. J. Wagg, "Dynamic analysis of high static low dynamic stiffness vibration isolation mounts," *Journal of Sound and Vibration*, vol. 332, no. 6, pp. 1437–1455, 2013.

[66] Z. Zhao, R. Zhang, Y. Jiang, and C. Pan, "A tuned liquid inerter system for vibration control," *International Journal of Mechanical Sciences*, vol. 164, Article ID 105171, 2019.

[67] Y. Jiang, Z. Zhao, R. Zhang, D. De Domenico, and C. Pan, "Optimal design based on analytical solution for storage tank with inerter isolation system," *Soil Dynamics and Earthquake Engineering*, vol. 129, Article ID 105924, 2020.

[68] R. Zhang, Z. Zhao, and K. Dai, "Seismic response mitigation of a wind turbine tower using a tuned parallel inerter mass system," *Engineering Structures*, vol. 180, pp. 29–39, 2019.

[69] Y. Wang, Z. Chen, C. Yang, Z. Liu, J. He, and Z. Feng, "A novel eddy current damper system for multi-mode high-order vibration control of ultra-long stay cables," *Engineering Structures*, vol. 262, Article ID 114319, 2022.